Composite Structures 132 (2015) p. 864-873.
DOI: 10.1016/j.compstruct.2015.07.018

Full-field strain measurements and meso-FE modelling of hybrid carbon/self-reinforced polypropylene

Seyed Ahmad Tabatabaei[1], Yentl Swolfs[1*], Haoran Wu[1], Stepan V. Lomov[1]
[1] Department of Materials Engineering, KU Leuven, Belgium.
*Corresponding author. yentl.swolfs@mtm.kuleuven.be

Abstract

The strain fields in tension were investigated for hybrid carbon fibre/self-reinforced polypropylene (SRPP) composites. Polypropylene tapes were co-woven with carbon fibre prepreg tapes and hot compacted into composite plates. Digital Image Correlation (DIC) was employed to measure the local surface strains during uniaxial tension. The geometry of the hybrid composite was modelled using WiseTex software and transferred to Abaqus for meso-finite element (FE) modelling using the embedded element method. The comparison between experiments and calculated strain patterns confirmed the validity of the meso-FE modelling for this complex weave architecture. The details of the strain fields were revealed in the FE results, whereas the DIC analysis averaged them out. This strain field information provides a foundation for the analysis of synergetic effects in hybrid composites.

Keywords: Meso-finite element modelling; Embedded element method; Self-reinforced composites, Digital image correlation; Hybrid composites.

1 Introduction

Self-reinforced composites (SRCs) consist of oriented polymer fibres or tapes in an isotropic matrix of the same polymer. In comparison to traditional fibre-reinforced composites, SRCs are tougher, easier to recycle and have a better bonding between fibre and matrix [1-4]. Hot compaction is one of the common processes to make SRCs [2, 5, 6]. In this process, the outer sheath of the fibre/tape melts and recrystallises to form the matrix upon cooling. The inner core of the fibres/tapes maintains high molecular orientation and acts as reinforcement [2, 6]. While SRCs possess excellent impact resistance, they are not stiff enough for structural applications. Such an issue is typically resolved by adding carbon fibres in the composite [7-14]. For SRC hybrids, intralayer hybrids of carbon fibre polypropylene (CFRPP) and self-reinforced polypropylene (SRPP) have proven to be a particularly successful combination [12, 15]. In such hybrids, CFRPP prepregs are co-woven with polypropylene (PP) tapes. After compaction, a CFRPP/SRPP hybrid composite is obtained.

The SRPP weave architecture is already complex due to the partial folding of the tapes [16]. The addition of CFRPP prepreg tapes makes this architecture even more complicated [12]. The damage development in these hybrid composites is hence complex and can involve synergetic effects between CFRPP prepregs and PP tapes [17, 18]. The damage mechanisms are a combination of debonding, delamination and damage within the PP tapes and CFRPP prepregs [12]. These damage mechanisms cause changes in the local strains, which are crucial in understanding the overall behaviour of the hybrid composite. Digital Image Correlation (DIC) can be used to gain more insight into the complex distribution of local strains. However, DIC can only measure surface strains, which are not necessarily the same as the internal strains due to

Composite Structures 132 (2015) p. 864-873.
DOI: 10.1016/j.compstruct.2015.07.018

the complex architecture. DIC can however be a tool to validate models that do predict these internal strain distributions [19-21]. So far, DIC has not been applied yet to study strain fields in hybrid composites that contain yarns with very different stiffnesses. In this situation, high strain gradients are expected at the edges of the yarns.

Therefore, meso-finite element modelling (FEM) is essential to understand and predict the composite mechanical properties and damage development [22-24]. The complex weave architecture however introduces two serious issues in traditional meso-FEM with continuous meshes in reinforcement and matrix regions: quality meshing of the matrix pockets [25] and elimination of yarn interpenetration [24, 26]. The weave architecture of intralayer hybrid CFRPP/SRPP is especially difficult to handle because of the high weave density and the additional interactions with the CFRPP prepregs. The embedded element method [27-31] and its analogues, such as superimposed meshes, independent meshes and M^3 [32-35], can deal with these issues in a reliable manner. It has never been applied to hybrid textile composites, where its advantages can be decisive in the formulation of a solvable FE problem.

This study is part of a larger one aiming to fully understand and predict mechanical properties and damage development in SRPP/CFRPP hybrid composites [11-15]. Here, the elastic behaviour of these hybrid composites is analysed in uniaxial tension. The stiffness and strength as well as strain patterns are obtained from tensile tests combined with DIC. The geometry of the complex weave architecture of SRPP/CFRPP is measured and converted into a geometric unit cell model by WiseTex [36, 37]. This geometry is then meshed and modelled using the embedded element method in Abaqus. The meso-FE unit cell is loaded in the warp and weft direction and the predicted strain profiles are compared to experimental results.

2 Materials and experimental methods

2.1 Materials

Polypropylene (PP) tapes were provided by Propex Fabrics GmbH (Germany). These tapes were drawn 10-15 times, and had a linear density of 110 tex. Unidirectional CFRPP prepregs were sourced from Jonam Composites (UK). Their microstructure is revealed in Fig. 1. The thickness and width of these prepregs was 160 µm and 100 mm respectively. They were slit into tapes with a width of 2.5 mm. The volume fraction of the T700S carbon fibre in the prepreg was determined to be 32% using the matrix burn off method [12].

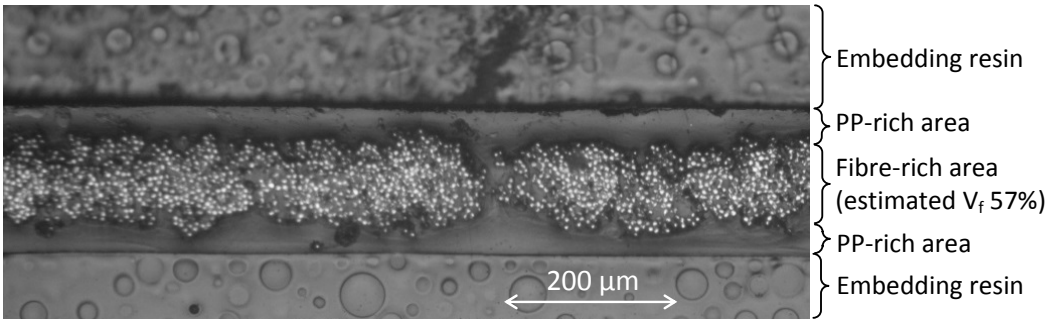

Figure 1: Microstructure of the CFRPP prepreg tape with PP-rich areas at the top and bottom of the prepreg.

Composite Structures 132 (2015) p. 864-873.
DOI: 10.1016/j.compstruct.2015.07.018

Propex Fabrics GmbH weaved the CFRPP prepregs into a hybrid fabric cloth that can be understood as a modified twill 2/2 weave of PP tapes. This twill architecture was modified by replacing one out of every six PP tapes in the weft direction by a CFRPP prepreg tape (see Fig. 2a). The prepregs were, however, only interlaced with the PP tapes every four tapes. This puts the prepreg tapes more towards one side of the fabric (see Fig. 2a and b). As can be seen in the inset of Fig. 2a, the PP tapes did not all have the same width: some tapes were approximately two times wider than others. This is explained by folding of the tapes during the weaving process [16]. All the PP weft tapes are folded. The PP warp tapes that were interlaced with CFRPP tapes were folded, whereas the uninterlaced warp PP tapes were not folded (see Fig. 2a).

The weave of the PP tapes was very dense, as both the warp and weft tapes overlapped with their neighbours. During hot compaction, the outer layer of these tapes melts and forms the matrix of the self-reinforced composite. The core of the tapes will not overlap anymore and form the final reinforcement architecture. As will be explained later, all these features were taken into account in the geometric model of the composite.

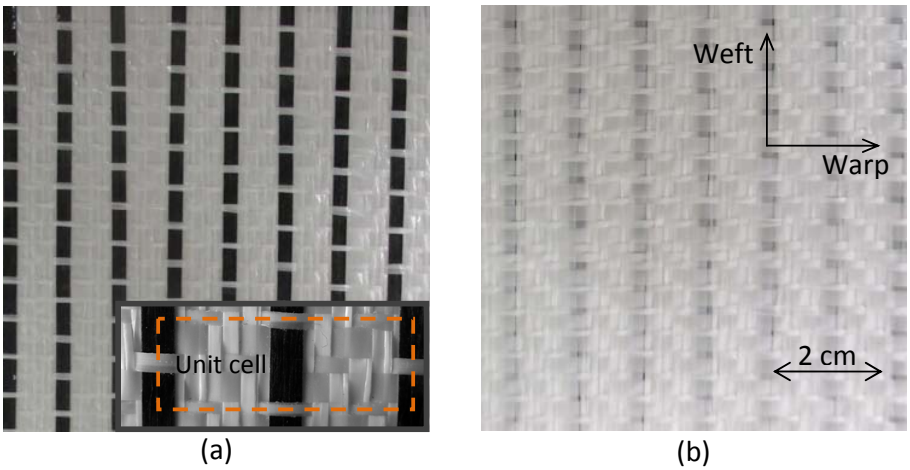

Figure 2: The hybrid SRPP/CFRPP fabric: (a) front side with the CFRPP prepregs clearly visible, and (b) back side with the CFRPP prepregs shining through. The dashed rectangle in the inset represents the unit cell of the weave.

2.2 Production

Eight woven C/PP layers of 320×320 mm were stacked in $(0/90/0/90)_s$ layup, where "0" or "90" designates the orientation of the CFRPP tapes. The prepreg sides of the hybrid fabrics were always placed towards the closest outside of the layup to ensure a symmetric configuration. This means that the four bottom layers had the prepregs facing downwards, whereas they faced upwards for the four top layers. The layup was placed in between two aluminium cover plates and put into a pre-heated hot press. The compaction temperature of 188°C was applied for 5 min, after which the press cooled down to room temperature in 5 min. The applied pressure was 3.9 MPa throughout the process.

The carbon fibre volume fraction V_f in the compacted sheets was calculated as follows. A 100 cm² specimen of the hybrid fabric was weighed. The prepregs were then carefully

Composite Structures 132 (2015) p. 864-873.
DOI: 10.1016/j.compstruct.2015.07.018

drawn out of the fabric and weighed separately. These measurements are combined with a density of 920 kg/m³ for PP, 1800 kg/m³ for carbon fibre and the measured V_f of the prepregs. This calculation resulted in a carbon fibre volume fraction of 7% for the hybrid composite. The calculation requires the assumption that no PP is lost during compaction. This is realistic, as no material flows out during production.

2.3 Tensile tests and full-field strain measurement

Tensile tests were performed according to the ASTM D3039 standard. The specimens were cut in the 0° and 90° direction in relation to the direction of the CFRPP tapes on the surface of the plate. The 250×25 mm composite samples were water jet cut and sprayed with white and black acrylic spray over a length of 75 mm. The obtained speckle pattern will be used to perform DIC. Five tensile tests were performed in both directions using an Instron 4505 tensile machine with a load cell of 100 kN. The X direction refers to the orientation where the outer CFRPP prepreg tapes were aligned with the tensile specimen. The Y direction refers to the orientation where the outer CFRPP tapes were perpendicular to the loading direction. The surface strain fields in both directions can significantly differ, even though the tensile properties are expected to be similar.

Sand paper was used to ensure sufficient friction between the specimen and the grips. The gauge length was 150 mm, and the specimens were tested at a strain rate of 5 %/min. Every 500 ms, an image of the tensile specimen was taken. All strain fields were correlated using Limess Vic2D 2009 at a subset and step size of 15 and 3 pixels respectively.

The strain was registered using DIC until failure of the CFRPP prepreg tapes. When they failed catastrophically, the surface of the specimen was severely damaged. After this point, the DIC strain measurements were not reliable anymore. The approach described by Swolfs et al. [12, 15] was used for estimating the strain afterwards. The average surface strain was used until failure of the CFRPP, after which the strain is calculated from the corrected crosshead displacement. This was found to be a reliable and efficient approach for hybrid self-reinforced composites. The tensile modulus was calculated from the slope of the stress-strain curve for strains ranging from 0.8% to 1%. This was necessary to avoid the initial non-linearity, caused by straightening of the CFRPP tapes in a compliant PP matrix.

2.4 Geometric model of the hybrid fabric

The geometric model of the reinforcement was built using the WiseTex software [36, 37]. The input data was acquired using measurements of the reinforcement geometry and is shown in Table 1. The yarn dimensions, ends and picks count were measured on the hybrid fabric (see Fig. 2). The thickness of the CFRPP prepregs in the compacted sheet was measured on cross-sectional microscopy images. The width was measured on the surface of the compacted specimens. The thickness of the remaining PP tapes after hot compaction was adjusted, so that the thickness of the reinforcement layer in the sheet agrees with the measured value of the sheet thickness. It was assumed that the yarn spacing was not changed during hot compaction. The tape core area after compaction was assumed to be 80% of the cross section area of the PP tape [38, 39]. The width of the core of the PP tapes was calculated based on the tape core area and

Composite Structures 132 (2015) p. 864-873.
DOI: 10.1016/j.compstruct.2015.07.018

thickness. The slight differences between the geometry of the hybrid fabric before hot compaction and the reinforcement geometry of the compacted sheet are shown in Table 1.

Due to overfeeding of the PP tapes during weaving [16], some PP tapes were partially folded. Therefore, narrow and wide PP tapes were present in the hybrid fabric. The width of narrow PP tapes was measured to be 1.75 times less than the width of unfolded tapes. The same ratio was maintained in the geometric model. The CFRPP prepreg tapes and the narrow PP tapes were assumed to have elliptical cross-sections, whereas the cross-section of the wide PP tapes was assumed to be rectangular. The volume fraction of carbon fibres inside the prepreg tapes after hot compaction was estimated using the measured overall V_f of the carbon fibres in the fabric combined with the V_f of the CFRPP tapes in the fabric. The latter was determined by their dimensions and picks count. The carbon fibre volume fraction inside the prepreg tapes in the compacted sheet was estimated to be 57%. This value differs from the V_f in the prepreg tape before weaving and compaction (32%) because of the resin-rich zones on the surface of the prepregs (see Fig. 1). These zones will end up as matrix in the hybrid composite and cannot be distinguished from the rest of the matrix material.

The geometric model of the hybrid composite was built based on the twill 2/2 PP tape weave pattern. One out of every six PP tapes in the weft direction was replaced by a CFRPP prepreg. This CFRPP prepreg was interlaced with the twill 2/2 pattern only once out of every four warp PP tapes. The modelled geometry (see Fig. 3) corresponds as accurately as possible to the one shown in the inset of Fig. 2a. Note that the exact position of the PP tapes in the actual fabric does deviate from the average position.

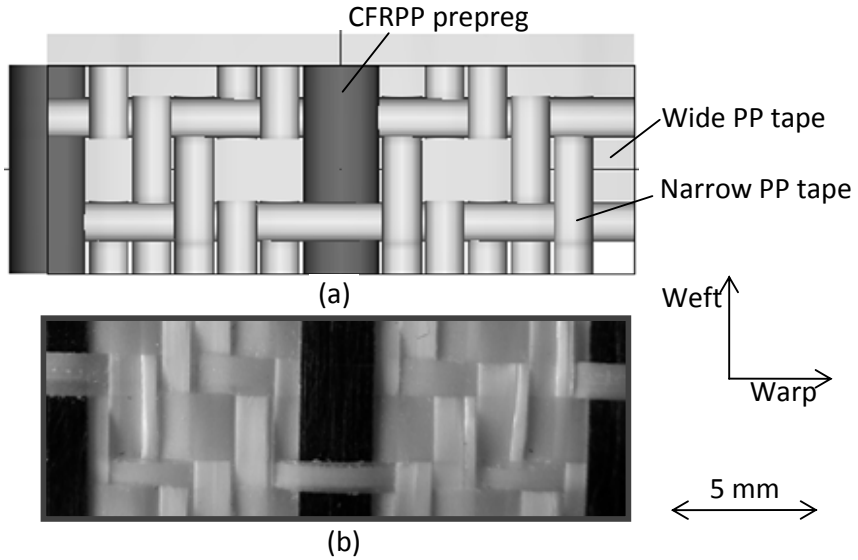

Figure 3: The unit cell of the hybrid fabric: (a) geometric unit cell built by WiseTex, and (b) photograph of the real unit cell.

Composite Structures 132 (2015) p. 864-873.
DOI: 10.1016/j.compstruct.2015.07.018

3 Finite element model

The WiseTex geometric model of the hybrid self-reinforced composite (see Fig. 3a) was transferred to Abaqus using a Python script. Then, the embedded element (EE) method was applied for meso-FE modelling.

The 1, 2, 3 directions in the local coordinate system of the warp yarns are along the X, -Y and -Z directions in the global coordinate system. In the weft yarns, the 1, 2, 3 directions correspond to the X, Y, Z directions in the global coordinate system.

A small volume loss occurs during the transfer of the geometric model to Abaqus. This is a result of the approximate representation of the cross-sectional geometry after replacement of elliptical contours with a set of straight boundaries of the elements. The fibre volume fraction V_f in the yarns should therefore be corrected based on the following relation:

$$\mathbf{V_f(Abaqus) = \frac{V_R(Abaqus)}{V_U} \times \frac{A_Y(Abaqus)}{A_Y(WiseTex)}}, \quad (1)$$

where V_f is the fibre volume fraction in the yarns after transferring to Abaqus, V_R is the overall volume of the reinforcement in Abaqus, V_U is the total volume of the unit cell, and A_Y is the cross-sectional area of a single yarn. Values for V_f(Abaqus) were used for calculation of the homogenised yarn properties.

The EE method is based on mesh superposition: the matrix (host part) and reinforcement (embedded part) are meshed separately, but the meshes are superimposed onto each other [40]. The translational degrees of freedom of the embedded part are related to the translational degrees of freedom of the host part using the weighted average functions [27, 41].

The embedded element method leads to a good quality mesh in the matrix and in the yarns and solves the interpenetration problem [24] by applying a contact constraint between the reinforcement parts [28, 31]. In this study, the "surface-to-surface" contact algorithm with "node adjustment" was applied. The volume redundancy effect in the superimposed regions was compensated as follows [31]:

$$\left[\mathbf{D}_{emb}\right] = \left[\mathbf{D}_{r}\right] - \left[\mathbf{D}_{m}\right] \quad (2)$$

where $\left[\mathbf{D}\right]$ was the constitutive stiffness matrix for the reinforcement "r", elements in the embedded region "emb" or matrix "m". The stress components in the reinforcement were recalculated during post-processing as:

$$\left\{\boldsymbol{\sigma}_{f}\right\} = \left[\mathbf{D}_{r}\right]\left\{\boldsymbol{\varepsilon}_{emb}\right\} \quad (3)$$

where ε_{emb} were the strains calculated in the embedded region.

Fig. 4 shows the meshed unit cell of the hybrid composite. The unit cell, constructed based on the geometric WiseTex model, consists of a single layer while the real

Composite Structures 132 (2015) p. 864-873.
DOI: 10.1016/j.compstruct.2015.07.018

configuration has eight layers in a $(0/90/0/90)_s$ layup. Therefore, the unit cell of one layer was repeated in the X, Y, and Z directions to create a unit cell of four layers with overall dimensions of 19.2×19.2×0.855 mm. The Z+ surface of the unit cell was traction-free, whereas symmetry conditions were applied to the Z- surface, representing eight layers of the actual layup. Periodic boundary conditions were applied to the unit cell along the X and Y directions (see Fig. 4c). The in-plane homogenised stiffness properties were calculated by applying X-tension, Y-tension and XY-shear displacement boundary conditions to the unit cell. The FE results were compared with stiffness calculations using the classical laminate theory (CLT). In the CLT calculations, all yarns were represented with unidirectional flat plies with the volume fractions corresponding to the yarn volume in the real laminate.

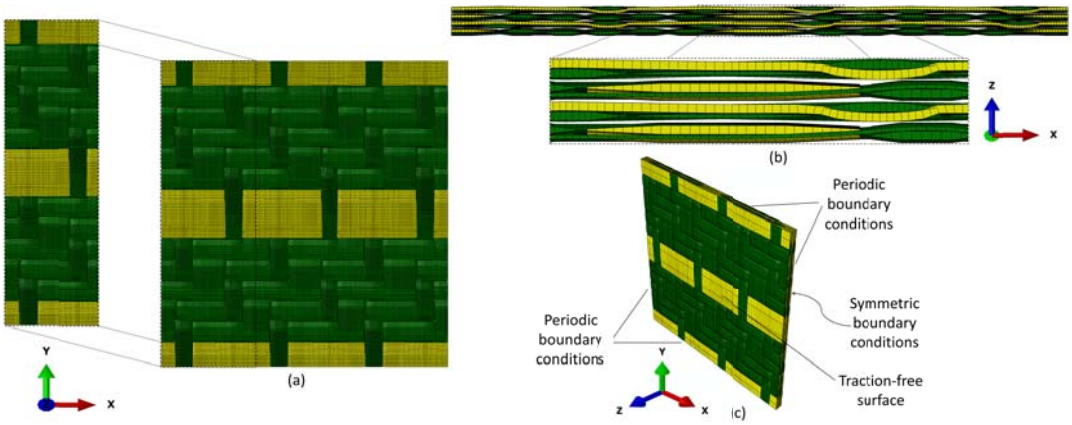

Figure 4: The meso-FE model for the hybrid SRPP/CFRPP composite using the embedded element method: (a) a unit cell showing how it is repeated to obtain the meso-FE model, (b) side view of the four stacked layers of yarns, and (c) the applied boundary conditions.

The engineering constants of the PP tape, PP matrix and carbon fibre are shown in Table 2. Based on this information and a 57.2% fibre volume fraction of carbon fibres inside the prepreg tapes, the homogenised properties of the CFRPP prepreg were calculated using Chamis' formulae [42]. The stiffness of the PP core tapes in the compacted composite was knocked down from 10 to 8 GPa to account for relaxation during hot compaction [38].

4 Results and discussion

4.1 Experimental results

A representative stress-strain diagram and the corresponding strain fields are shown in Fig. 5 and Fig. 6 for loading in the X and Y direction, respectively. The overall behaviour is similar to that reported by Swolfs et al. [12]. At about 2% strain, the CFRPP prepregs fail, which causes the prepreg tapes to partially debond and leads to a vertical stress drop. At higher strains, the prepreg tapes debond further until they are completely debonded at a strain of 12%. In the final part, the CFRPP is not contributing to the stress transfer anymore and the SRPP fails at its usual failure strain of 17-20%.

Fig. 5 and Fig. 6 also contain the strain field at three different strains. The first strain field (see Fig. 5b and Fig. 6b) corresponds to a stress level of about 60 MPa and a strain

Composite Structures 132 (2015) p. 864-873.
DOI: 10.1016/j.compstruct.2015.07.018

of about 1%. This level is well before failure of the CFRPP tapes. The second strain field (see Fig. 5c and Fig. 6c) is the one just before failure of the CFRPP tapes. The third and final strain field (see Fig. 5d and Fig. 6d) was taken after the failure of the CFRPP tapes. At this point, the sample surface is damaged, causing DIC to lose the correlation. The two strain fields at lower overall strain, however, do reveal periodic strain patterns.

The difference between X and Y loading stems from the orientation of the CFRPP prepreg tapes at the surface. In X loading, these tapes are oriented in the loading direction, whereas they are transverse to the loading direction for Y loading. The difference in strain pattern hence stems from the different orientation of the outer ply. In X loading, the high strain regions correspond to locations where the CFRPP tape is underneath a PP tape. This yields higher strains, as the lower stiffness material is on the surface. The lower strain regions correspond to locations where the CFRPP is on top of the PP tapes. Similarly, this yields lower strains, as the higher stiffness material is on the surface this time.

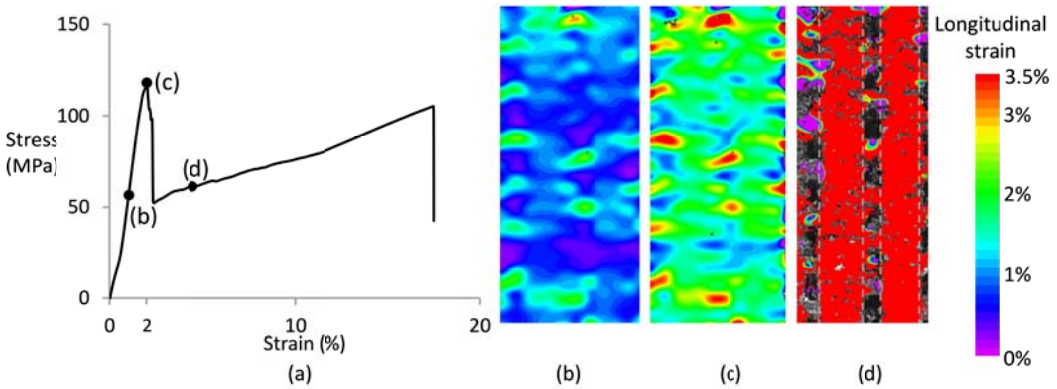

Figure 5: Behaviour of hybrid SRPP/CFRPP loaded in the X direction: (a) representative stress-strain diagram, (b) strain field at a stress of 60 MPa, (c) strain field just before CFRPP failure, and (d) strain field after CFRPP failure. Only pixels that could be correlated are in colour. The edges of the CFRPP yarns are indicated by a grey dashed line in (d).

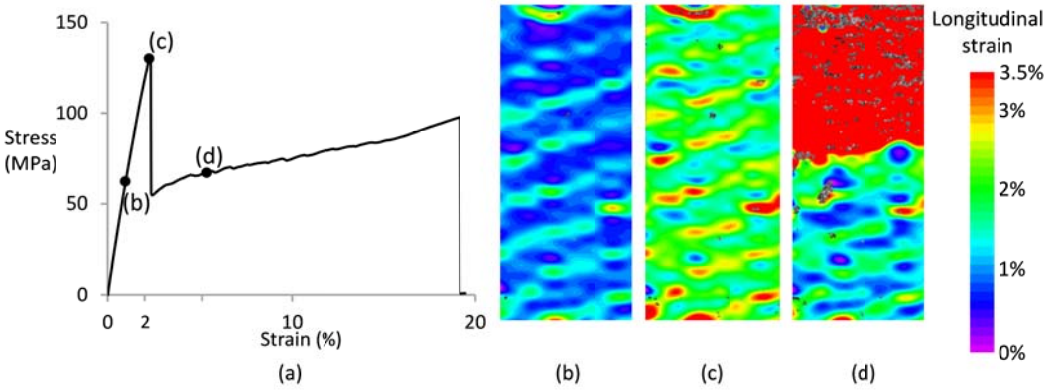

Figure 6: Behaviour of hybrid SRPP/CFRPP loaded in the Y direction: (a) representative stress-strain diagram, (b) strain field in the linear elastic regime, (c) strain field right before CFRPP failure, and (d) strain field after CFRPP failure. Only pixels that could be correlated are in colour.

Composite Structures 132 (2015) p. 864-873.
DOI: 10.1016/j.compstruct.2015.07.018

The tensile modulus in the elastic region of the stress-strain curve was 5.4 $\pm$ 1.6 GPa and 6.1 + 0.3 GPa for the X and Y direction respectively. A t-test revealed that these values are not significantly different from each other (p-value of 38%). This is expected as the $(0/90/0/90)_s$ should lead to very similar properties in both directions. However, a slightly higher modulus in the Y direction can be expected, because of the lower contribution of the outer ply to the overall stiffness [43].

Fig. 7 plots the longitudinal surface strain profiles along a CFRPP yarn in the X and Y loading directions. In both cases, the profile path is parallel to the loading direction. The location where these profiles were taken from, are indicated on the unit cell (see arrows on the insets in Fig. 7). The figure shows a typical profile from one of such locations. Both loading conditions reveal a periodic pattern, although the periodicity is more pronounced for the X loading direction. For the Y loading, the periodicity is less precise due to variations of the exact location of the CFRPP tapes.

The peaks and valleys are likely to be related to the architecture of the hybrid fabric, as indicated in Fig. 7. The average distance between the peaks for X loading is 7.9 cm, which roughly corresponds to the periodicity of the unit cell. The peaks correspond to the locations of the compliant PP tapes over the CFRPP tapes, as shown in Fig. 7. The minima of the strain profiles for loading in the Y direction correspond to the positions in between the cross-over points of the CFRPP tapes.

Composite Structures 132 (2015) p. 864-873.
DOI: 10.1016/j.compstruct.2015.07.018

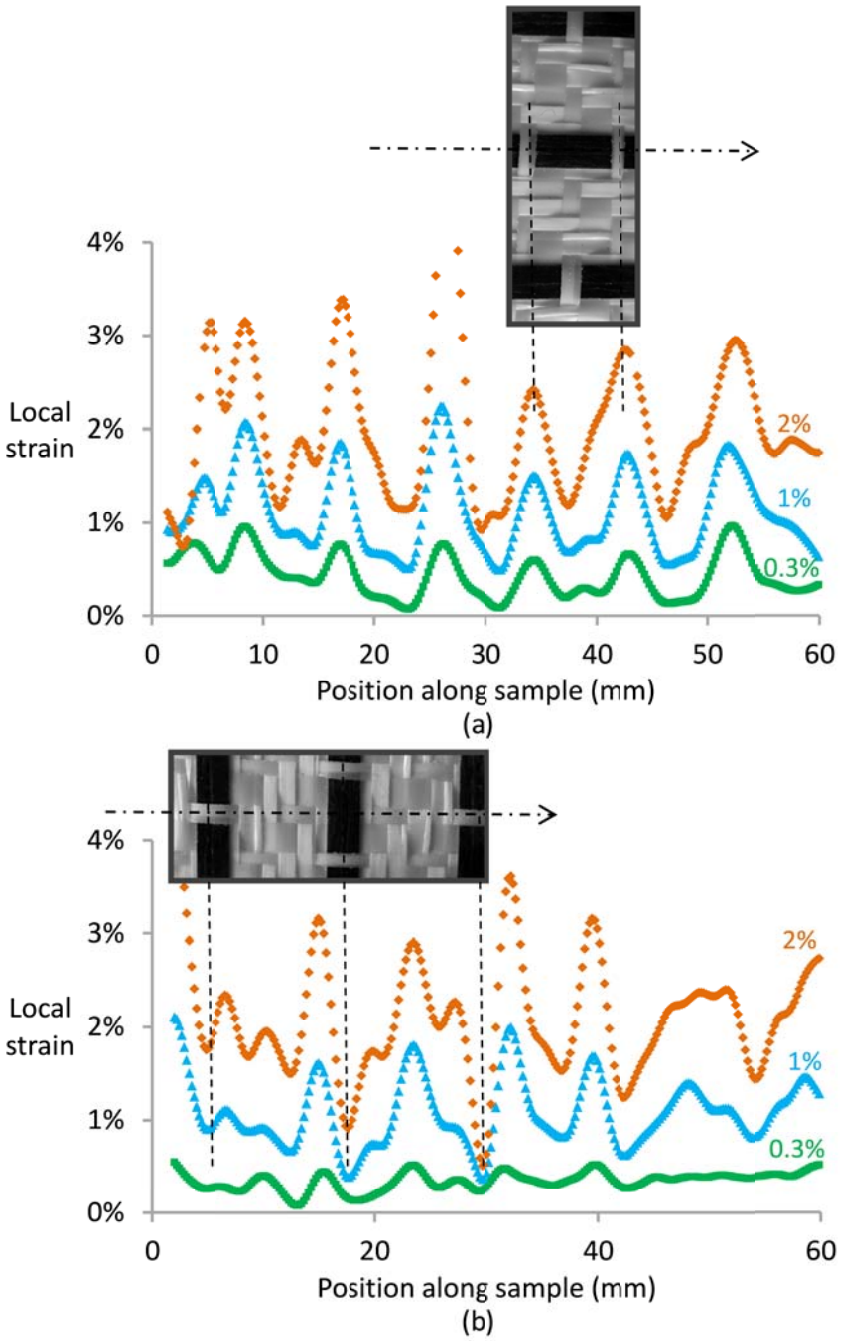

Figure 7: Longitudinal surface strain profiles along the length of the tensile sample: (a) X direction, and (b) Y direction. The profiles for three overall strain levels are plotted: 0.3%, 1% and 2%.

The linearity of the surface strain profiles evolution in the elastic deformation regime is confirmed in Fig. 8, which shows the strain profiles corresponding to three values of the applied strain, scaled according to the applied strain. The strain profiles indeed scale linearly with the applied strain. Some of the minor trends are not captured entirely. This may be related to the non-linearity that was observed in the stress-strain diagram. This non-linearity was attributed to straightening of the CFRPP tapes in a compliant PP matrix.

Composite Structures 132 (2015) p. 864-873.
DOI: 10.1016/j.compstruct.2015.07.018

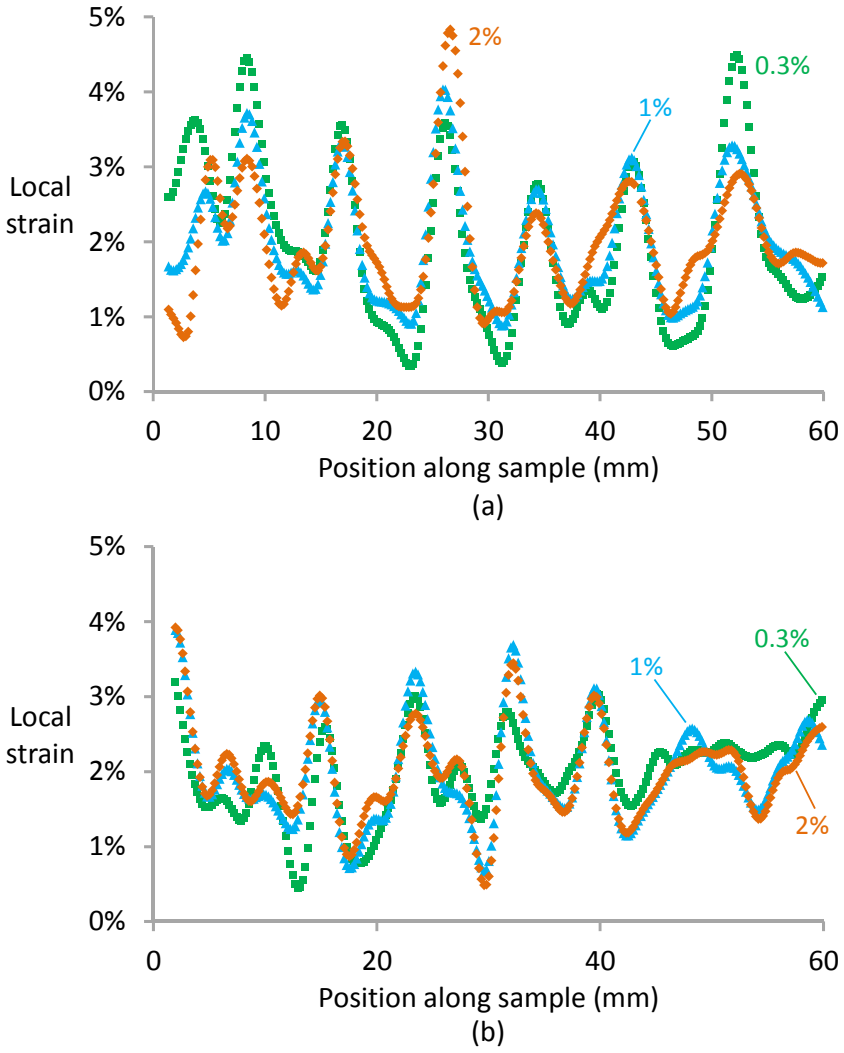

Figure 8: Strain profiles normalised to a strain of 2%: (a) for X loading, and (b) for Y loading.

4.2 Comparison with model results

The in-plane homogenised properties of the meso-FE model were calculated using the periodic boundary conditions applied in the three in-plane load cases and are shown in Table 3. Swolfs et al. [12] has already applied the classical laminate theory (CLT) to the same $(0/90/0/90)_s$ layup. The obtained value was added to Table 3. The main difference between both predictions was that CLT ignored the yarn crimp and hence overestimated the stiffness. This had only a minor influence on the stiffness predictions, as the maximum crimp of CFRPP tapes was 0.6%.

The homogenised Young's moduli in both directions (see Table 3) are significantly higher than the experimental results: 5.4 $\pm$ 1.6 GPa and 6.1 + 0.3 GPa for the X and Y directions, respectively. As shown by Swolfs et al. [12, 15], this difference is due to the fibre undulations that are inevitable during hot compaction. CLT and the meso-FE model do not incorporate these undulations, and therefore overestimate the stiffness.

Composite Structures 132 (2015) p. 864-873.
DOI: 10.1016/j.compstruct.2015.07.018

The strong molecular orientation of the PP tapes results in a tendency to shrink at high temperatures [44]. This puts compressive stresses on the carbon fibres, leading to fibre undulations.

The strain patterns in the matrix, warp, and weft yarns for the meso-FE unit cell of the hybrid composite are shown in Fig. 9, Fig. 10 and Fig. 11 for an applied strain of 1%. When comparing these patterns to the experimentally measured strain patterns (see Fig. 5 and Fig. 6), one has to remember that the simulated patterns were calculated for a periodic and idealised layup with boundary conditions close to reality. The strain patterns for warp and weft yarns are shown for the outer layer in the meso-FE model. In the matrix, the strain patterns are shown at the traction-free surface.

The periodic strain patterns in the matrix, warp and weft yarns were captured in the meso-FE models (see Fig. 9). The main features in these patterns are related to the crossover points of the CFRPP. The less pronounced variations of the strain fields are related to PP tapes crossing over each other. This is for example clear for the ε_{xx}, ε_{yy} strains in X loading of the matrix (see Fig. 9a and c), where a stress variation is observed when the CFRPP tapes go over and under a PP tape. The zoom region in Fig. 9a reveals the tendency for the CFRPP tape to deform out of plane. This is a result of the applied load, which will tend to straighten the CFRPP tape. This pushes up the PP tapes that go over the CFRPP tapes (see Fig. 3). This can also be seen in ε_{zz} fields (see Fig. 9e). These deformations are possible due to the presence of the free surface, as explained by Ivanov et al. [43]. The out-of-plane deformations also affected the in-plane deformations, creating large strain variations at the same locations.

The magnitude of the strain variations is typically smaller for Y loading, as the load is applied perpendicular to the stiff CFRPP tapes. A peculiar pattern is observed in ε_{yy} (see Fig. 9d), as the strain patterns do not follow the periodicity of the outer layer. Instead, the periodic pattern is caused by the CFRPP tape in the second layer, as this tape is aligned with the loading direction. Its tendency to deform out-of-plane (see zoom region in Fig. 9d) causes the strain variations on the surface of the matrix. These variations are of the same nature as was explained above for the case of X loading. The amplitude of the strain variations was however smaller, as it was “covered” by the presence of the surface layer. This remarkable feature, which is clearly revealed by FE calculations using the full laminate layup, would be difficult to deduce from the experimentally registered strain profiles. One-layer FE simulations also would not reveal it.

The patterns observed in the matrix layer (see Fig. 9) are also visible in the warp (see Fig. 10) and weft yarns (see Fig. 11). The patterns of the yarn deformations in X loading are similar to those on the matrix surface. The out-of-plane deformations are better perceived from the matrix strain maps, where they are clearly localised on the bumps of PP tapes intersecting with CFRPP tapes. This feature can also be seen on the warp strain maps (Fig. 11a, c and e). The straightening of the CFRPP tape can be observed on the strain maps of the weft yarns (Fig. 10a, c and e). Y loading strain maps are again less characteristic, as the patterns reflect interaction of layers rather than yarn deformations in the outer layer.

Composite Structures 132 (2015) p. 864-873.
DOI: 10.1016/j.compstruct.2015.07.018

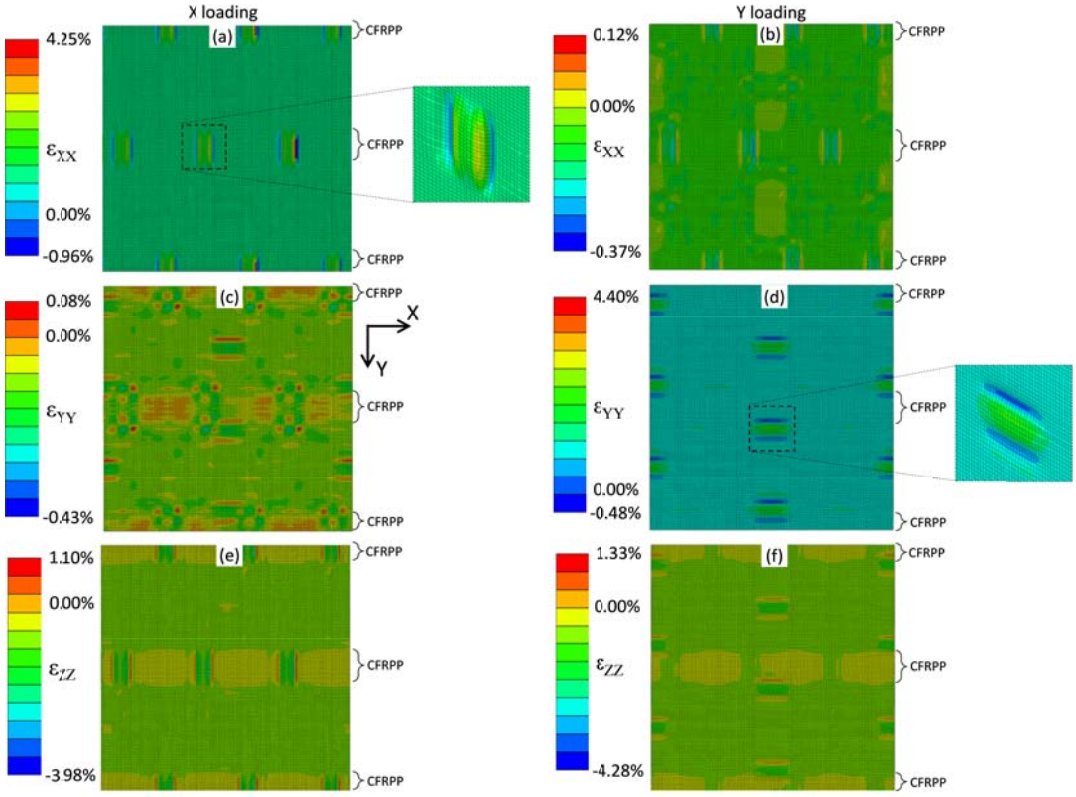

Figure 9: Strain patterns on the surface of the matrix layer, calculated by the meso-FE model at a global strain of 1%: (a) ε_{XX} in X loading, (b) ε_{XX} in Y loading, (c) ε_{YY} in Xloading, (d) ε_{YY} in Y loading, (e) ε_{ZZ} in X loading, (f) ε_{ZZ} in Y loading. The zoom regions in (a) and (e) are 3D representations showing the out-of-plane deformation. These deformations were magnified by a scale factor of 20 for the sake of clarity.

Composite Structures 132 (2015) p. 864-873.
DOI: 10.1016/j.compstruct.2015.07.018

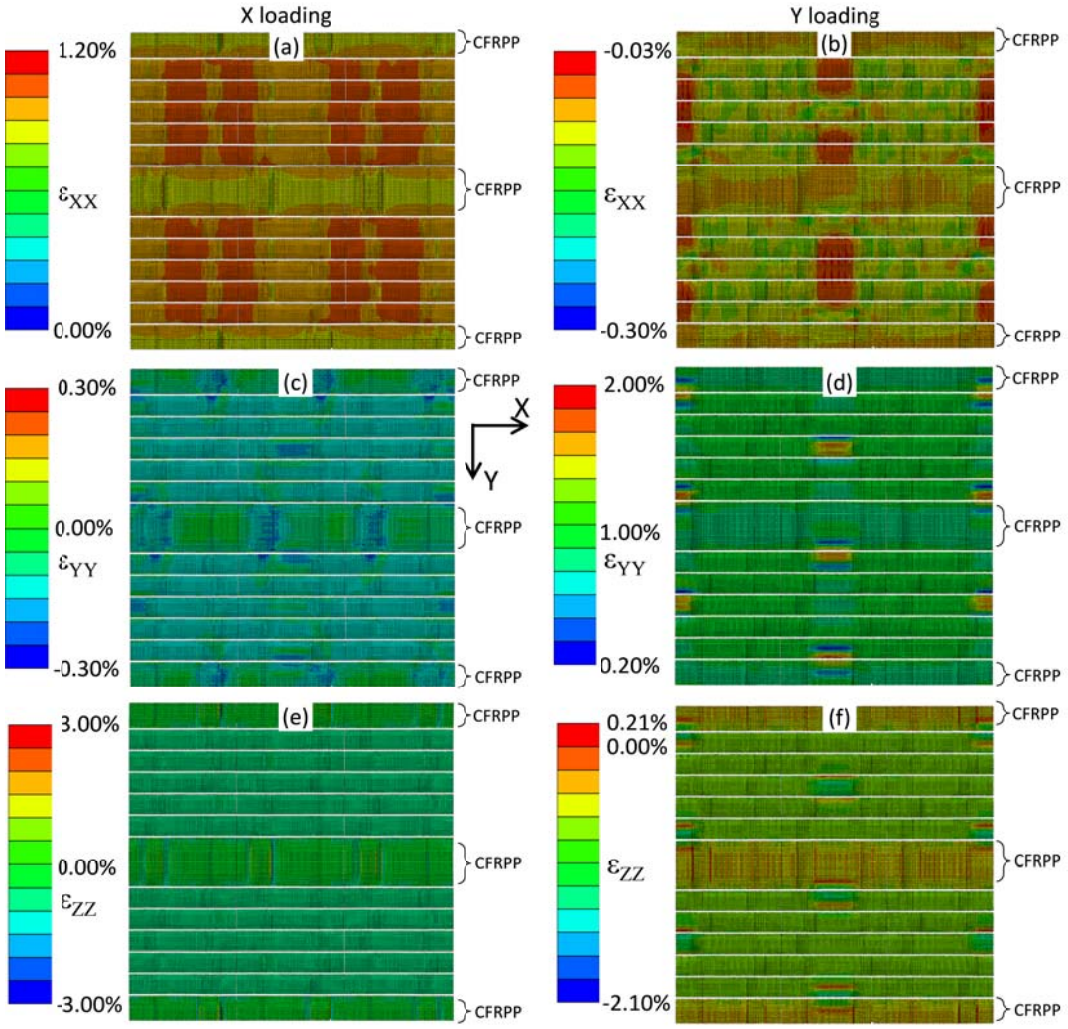

Figure 10: Strain patterns on the surface of the weft yarns, calculated by the meso-FE model at a global strain of 1%: (a) ε_{XX} in X loading, (b) ε_{XX} in Y loading, (c) ε_{YY} in X loading, (d) ε_{YY} in Y loading, (e) ε_{ZZ} in X loading, (f) ε_{ZZ} in Y loading.

Composite Structures 132 (2015) p. 864-873.
DOI: 10.1016/j.compstruct.2015.07.018

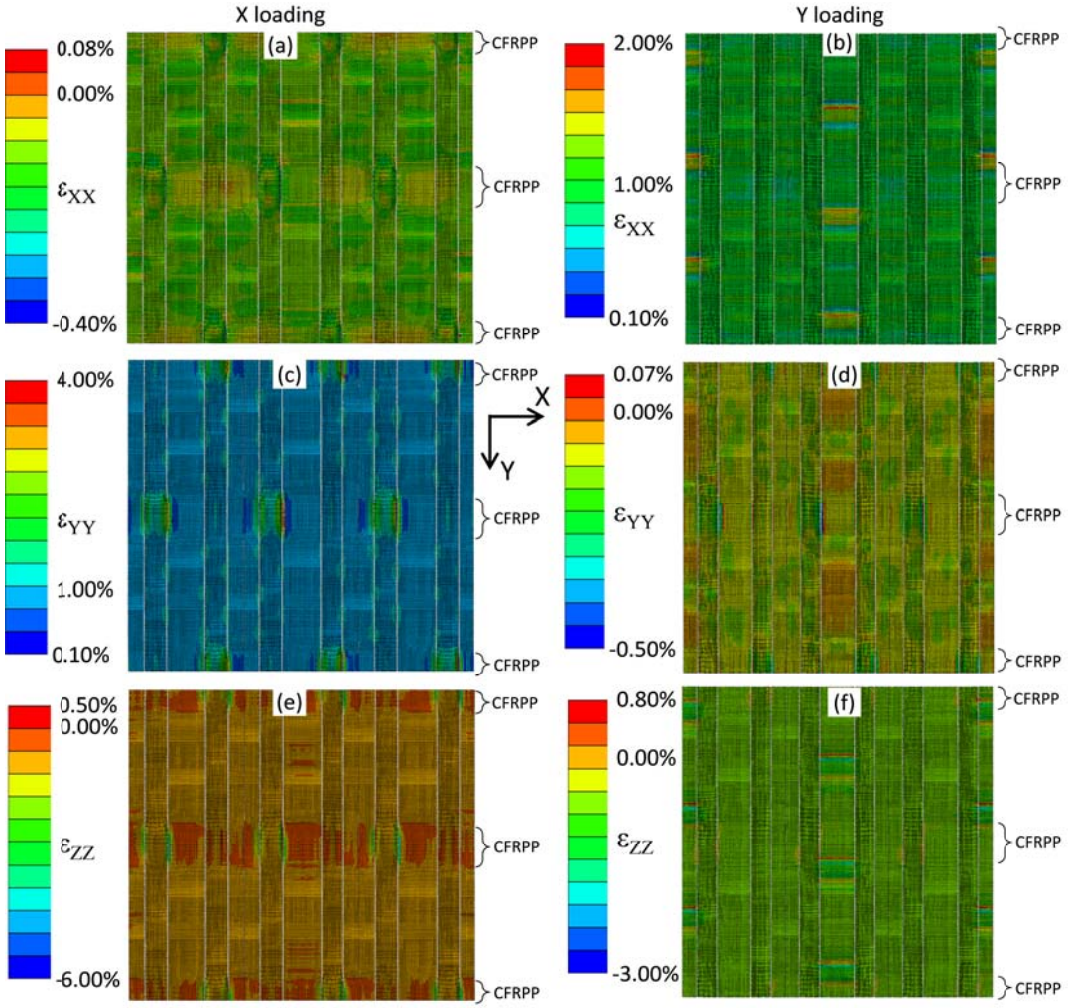

Figure 11: Strain patterns on the surface of the warp yarns, calculated by the meso-FE model at a global strain of 1%: (a) ε_{XX} in X loading, (b) ε_{XX} in Y loading, (c) ε_{YY} in X loading, (d) ε_{YY} in Y loading, (e) ε_{ZZ} in X loading, (f) ε_{ZZ} in Y loading.

Fig. 12 compares the surface strain profiles from the meso-FE model with those from experiments for loading in the X direction. The profiles were taken at the centre line of the CFRPP yarn. FE modelling correctly calculates the average strain, as prescribed by the boundary conditions. It also predicts the experimentally observed maximum of the strain at the position of intersection of CFRPP tape with PP yarn. The maximum strain corresponds to the CFRPP tape going underneath the warp PP yarns, leaving a low stiffness material on the surface of the specimen.

An important difference between the model and experiments is the local maxima and minima seen in the meso-FE model profiles. These are attributed to bending of the yarns, their non-flat sections and the presence of the matrix pockets close to the yarns. The two central peaks B and C in Fig. 12 correspond to the edge of a matrix pocket next to a PP tape crossing the CFRPP tape. The peaks A and D in Fig. 12 correspond to the

Composite Structures 132 (2015) p. 864-873.
DOI: 10.1016/j.compstruct.2015.07.018

highly bent region of the CFRPP tape. In these positions, the ε_{zz} strain is high (see Fig. 9e). DIC does not capture these variations of the strain fields due to (1) the averaging of strains over a relatively large subset of 15 pixel or 0.9 mm, and (2) the two-dimensional nature of the DIC measurement.

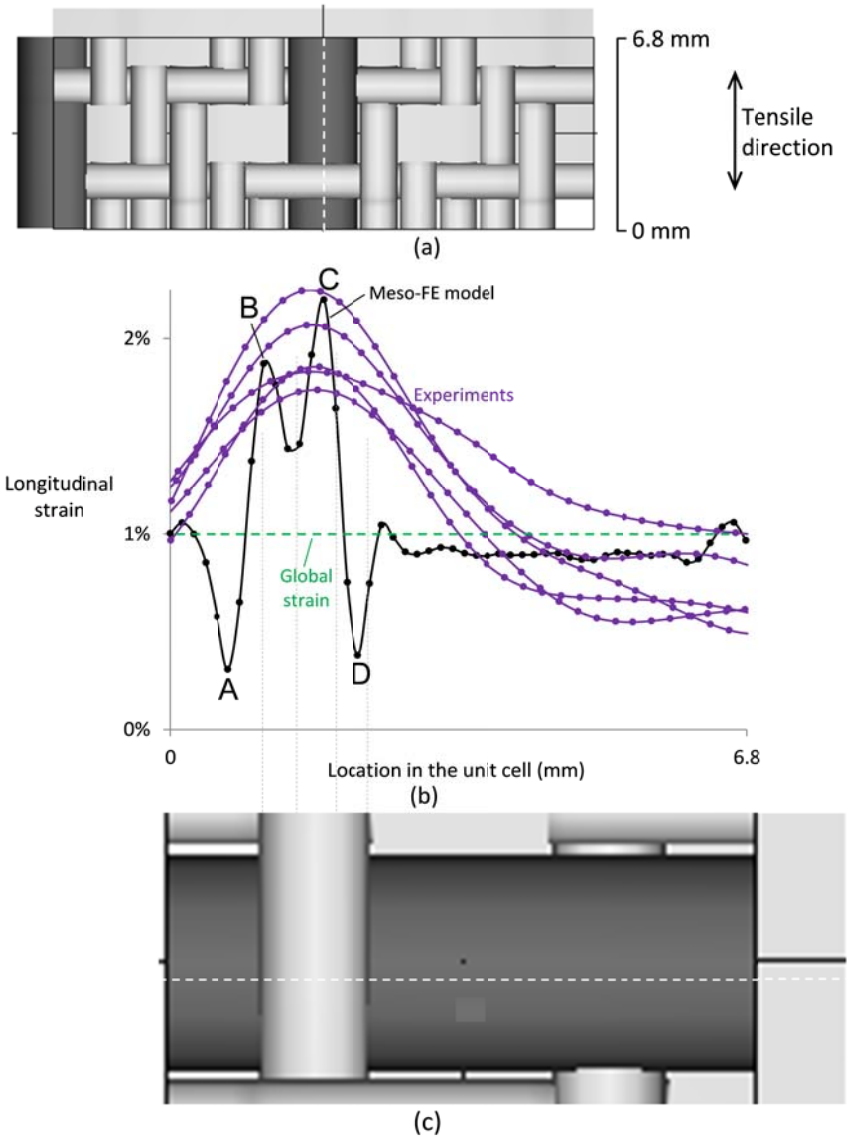

Figure 12: Comparison of the surface strain profiles between the meso-FE model and the experiments for loading in the X direction: (a) unit cell, the dashed line shows the strain profile path, (b) strain profiles in meso-FE model and experiments for three similar locations, and (c) detail of the unit cell showing where the meso-FE peaks are coming from.

Similar features, albeit not so strongly pronounced, were observed with high resolution phase-shifting shearography measurements of woven composites [45, 46], as well as in detailed DIC measurements [20, 21, 47]. These features have been also observed in meso-FE simulations for plain weave carbon and glass fibre composites [19, 20, 47, 48].

Composite Structures 132 (2015) p. 864-873.
DOI: 10.1016/j.compstruct.2015.07.018

Fig. 13 compares the surface strain profiles from the meso-FE model and experiments for loading in the Y direction. The locations of the peaks in the experiments correspond to the presence of the transverse CFRPP tapes. The meso-FE model however does not follow the same periodicity. The peaks in this case correspond to the underlying layer, with a periodicity of 6.8 mm. As explained earlier, the CFRPP tapes in this underlying layer deform out-of-plane, thereby causing in-plane deformations in the outer layer. The meso-FE was able to capture these, whereas they were averaged out in the DIC analysis. This proves the complementarity of DIC with meso-FE analysis.

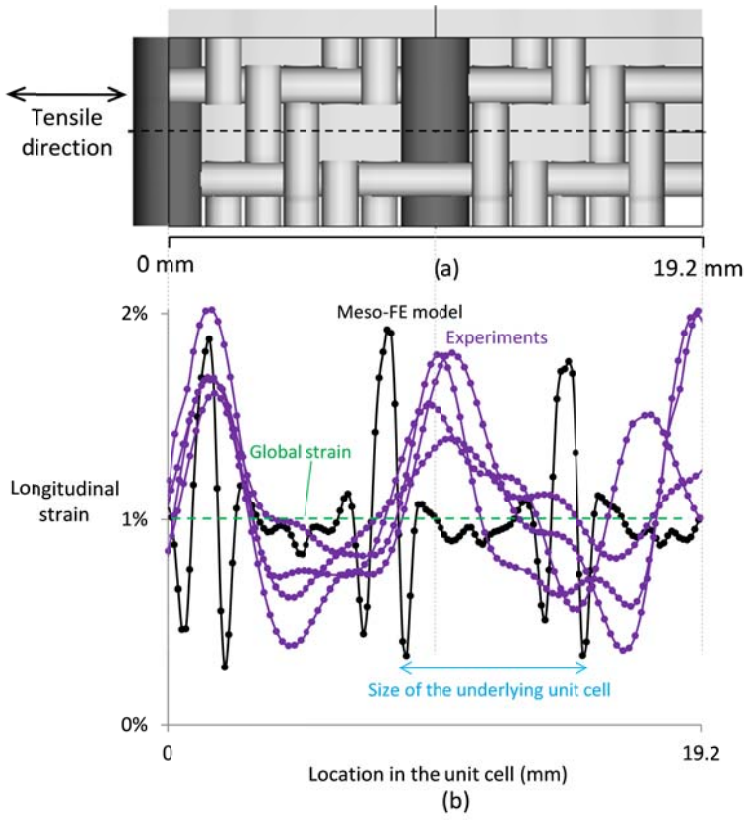

Figure 13: Comparison of the surface strain profiles between the meso-FE model and the experiments for loading in the Y direction: (a) unit cell, the dashed line shows the strain profile path, and (b) strain profiles in meso-FE model and experiments for three similar locations.

5 Conclusions

Full-field strain measurements were performed on SRPP/CFRPP hybrid composites under uniaxial tensile loading using DIC. The DIC results revealed periodic patterns at the surface of the SRPP/CFRPP fabric in which the peaks and valleys reflect the architecture of the hybrid fabric and the local stiffening of the composite by the CFRPP prepreg tapes.

The DIC results were compared to the results of meso-FE modelling, which used the embedded element method. The predicted stiffness agreed with the experimentally

measured values, taking into consideration fibre undulations due to shrinkage, which was neglected by the meso-FE model. The surface strain profiles revealed similar features in experiments and simulations on the length scale of the yarn width. The meso-FE model predicted additional features on a lower scale that were averaged out during the 2D DIC analysis. It was also more sensitive to out-of-plane deformations that were not captured in the DIC analysis.

Combining the embedded element method in meso-FE modelling with full-field strain mapping was found to lead to novel insights into the complex damage mechanisms of hybrid composites. This will be useful in analysing synergetic effects that often arise in hybrid composites, which is the next step in our study.

6 Acknowledgements

The work leading to this publication has received funding from the European Union Seventh Framework Programme (FP7/2007-2013) under the topic NMP-2009- 2.5-1, as part of the project HIVOCOMP (Grant Agreement n° 246389). The authors acknowledge the Agency for Innovation by Science and Technology in Flanders (IWT) for the grant of Y. Swolfs. S.V. Lomov is a Toray Professor (Toray Chair for Composite Materials, KU Leuven). The authors would like to thank Dr. K. Vallons for her help in the experimental tests.

7 References

[1] Alcock B, Peijs T. Technology and development of self-reinforced polymer composites. In: Abe A, Kausch HH, Moller M, Pasch H, editors. Polymer composites - polyolefin fractionation - polymeric peptidomimetics - collagens. Berlin: Springer-Verlag; 2013. p. 1-76.
[2] Ward IM, Hine PJ. The science and technology of hot compaction. Polymer. 2004;45(5):1413-27.
[3] Gao C, Yu L, Liu H, Chen L. Development of self-reinforced polymer composites. Progress in Polymer Science. 2012;37(6):767-80.
[4] Alcock B, Cabrera NO, Barkoula NM, Wang Z, Peijs T. The effect of temperature and strain rate on the impact performance of recyclable all-polypropylene composites. Composites Part B: Engineering. 2008;39(3):537-47.
[5] Kmetty Á, Bárány T, Karger-Kocsis J. Self-reinforced polymeric materials: A review. Progress in Polymer Science. 2010;35(10):1288-310.
[6] Swolfs Y, Zhang Q, Baets J, Verpoest I. The influence of process parameters on the properties of hot compacted self-reinforced polypropylene composites. Composites Part A: Applied Science and Manufacturing. 2014;65:38-46.
[7] Jawaid M, Khalil H. Cellulosic/synthetic fibre reinforced polymer hybrid composites: A review. Carbohydr Polym. 2011;86(1):1-18.
[8] Fiore V, Valenza A, Di Bella G. Mechanical behavior of carbon/flax hybrid composites for structural applications. Journal of Composite Materials. 2012;46(17):2089-96.
[9] Dong C, Davies IJ. Flexural strength of bidirectional hybrid epoxy composites reinforced by E glass and T700S carbon fibres. Composites Part B: Engineering. 2015;72(0):65-71.

[10] Sarasini F, Tirillo J, Ferrante L, Valente M, Valente T, Lampani L, et al. Drop-weight impact behaviour of woven hybrid basalt-carbon/epoxy composites. Composites Part B-Engineering. 2014;59:204-20.
[11] Hine PJ, Bonner M, Ward IM, Swolfs Y, Verpoest I, Mierzwa A. Hybrid carbon fibre/nylon 12 single polymer composites. Composites Part A: Applied Science and Manufacturing. 2014;65:19-26.
[12] Swolfs Y, Crauwels L, Van Breda E, Gorbatikh L, Hine P, Ward I, et al. Tensile behaviour of intralayer hybrid composites of carbon fibre and self-reinforced polypropylene. Composites Part A: Applied Science and Manufacturing. 2014;59:78-84.
[13] Verpoest I, Lomov S, Swolfs Y, Jacquet P, Michaud V, Manson J-A, et al. Advanced materials enabling high-volume road transport applications of lightweight structural composite parts. Sampe J. 2014;50(3):30-7.
[14] Swolfs Y, Meerten Y, Hine PJ, Ward IM, Verpoest I, Gorbatikh L. Introducing ductility in hybrid carbon fibre/self-reinforced composites through control of the damage mechanisms. Composite Structures. 2015;131:259-65.
[15] Swolfs Y, Shi J, Meerten Y, Hine P, Ward I, Verpoest I, et al. The importance of bonding in intralayer carbon fibre/self-reinforced polypropylene hybrid composites. Submitted to Composites Part A: Applied Science and Manufacturing. 2015.
[16] Swolfs Y, Crauwels L, Gorbatikh L, Verpoest I. The influence of weave architecture on the mechanical properties of self-reinforced polypropylene. Composites Part A: Applied Science and Manufacturing. 2013;53:129-36.
[17] Swolfs Y, Gorbatikh L, Verpoest I. Fibre hybridisation in polymer composites: a review. Composites Part A: Applied Science and Manufacturing. 2014;67:181-200.
[18] Kretsis G. A review of the tensile, compressive, flexural and shear properties of hybrid fibre-reinforced plastics. Composites. 1987;18(1):13-23.
[19] Daggumati S, Van Paepegem W, Degrieck J, Praet T, Verhegghe B, Xu J, et al. Local strain in a 5-harness satin weave composite under static tension: Part II - Meso-FE analysis. Composites Science and Technology. 2011;71(9):1217-24.
[20] Lomov SV, Ivanov DS, Verpoest I, Zako M, Kurashiki T, Nakai H, et al. Full-field strain measurements for validation of meso-FE analysis of textile composites. Composites Part a-Applied Science and Manufacturing. 2008;39(8):1218-31.
[21] Koohbor B, Ravindran S, Kidane A. Meso-Scale Strain Localization and Failure Response of an Orthotropic Woven Glass-Fiber Reinforced Composite. Composites Part B: Engineering. (0).
[22] Crookston JJ, Long AC, Jones IA. A summary review of mechanical properties prediction methods for textile reinforced polymer composites. Proceedings of the Institution of Mechanical Engineers Part L-Journal of Materials-Design and Applications. 2005;219(L2):91-109.
[23] Ansar M, Xinwei W, Chouwei Z. Modeling strategies of 3D woven composites: A review. Composite Structures. 2011;93(8):1947-63.
[24] Lomov SV, Ivanov DS, Verpoest I, Zako M, Kurashiki T, Nakai H, et al. Meso-FE modelling of textile composites: Road map, data flow and algorithms. Composites Science and Technology. 2007;67(9):1870-91.
[25] Hivet G, Boisse P. Consistent mesoscopic mechanical behaviour model for woven composite reinforcements in biaxial tension. Composites Part B: Engineering. 2008;39(2):345-61.

[26] Stig F, Hallström S. A modelling framework for composites containing 3D reinforcement. Composite Structures. 2012;94(9):2895-901.
[27] Abaqus 6.11 documentation.
[28] Tabatabaei SA, Lomov SV, Verpoest I. Assessment of embedded element technique in meso-FE modelling of fibre reinforced composites. Composite Structures. 2014;107(0):436-46.
[29] Matveeva AY, Pyrlin SV, Ramos MMD, Boehm HJ, van Hattum FWJ. Influence of waviness and curliness of fibres on mechanical properties of composites. Computational Materials Science. 2014;87:1-11.
[30] Romanov VS, Lomov SV, Verpoest I, Gorbatikh L. Modelling evidence of stress concentration mitigation at the micro-scale in polymer composites by the addition of carbon nanotubes. Carbon. 2015;82(0):184-94.
[31] Tabatabaei SA, Lomov SV. Eliminating the volume redundancy of embedded elements and yarn interpenetrations in meso-finite element modelling of textile composites. Computers & Structures. 2015;152:142-54.
[32] Kurashiki T, Fujita Y, Watanabe Y, Zako M. A Simulation on Damage Progression of Stitched Textile Composites Based on Multi-Scale Analysis. Lancaster: Destech Publications, Inc; 2010.
[33] Zako M, Kurashiki T, Kubo F, Imura M. A multi-scale analysis for structural design of fibrous composites – M3 method. In: Proceedings of Proceedings of the 15th International Conference on Composite Materials. Durban, Conference 2012, Conference 2005.
[34] Jiang WG, Hallett SR, Wisnom MR. Development of Domain Superposition Technique for the Modelling of Woven Fabric Composites. Mechanical Response of Composites: Springer Netherlands; 2008. p. 281-91.
[35] Iarve EV, Mollenhauer DH, Zhou EG, Breitzman T, Whitney TJ. Independent mesh method-based prediction of local and volume average fields in textile composites. Composites Part a-Applied Science and Manufacturing. 2009;40(12):1880-90.
[36] Verpoest I, Lomov SV. Virtual textile composites software WiseTex: Integration with micro-mechanical, permeability and structural analysis. Composites Science and Technology. 2005;65(15–16):2563-74.
[37] Lomov SV, Verpoest I, Cichosz J, Hahn C, Ivanov DS, Verleye B. Meso-level textile composites simulations: Open data exchange and scripting. Journal of Composite Materials. 2014;48(5):621-37.
[38] Swolfs Y, Van den fonteyne W, Baets J, Verpoest I. Failure behaviour of self-reinforced polypropylene at and below room temperature. Composites Part A: Applied Science and Manufacturing. 2014;65:100-7.
[39] Hine PJ, Ward IM, Jordan ND, Olley R, Bassett DC. The hot compaction behaviour of woven oriented polypropylene fibres and tapes. I. Mechanical properties. Polymer. 2003;44(4):1117-31.
[40] Fish J. The s-version of the finite element method. Computers & Structures. 1992;43(3):539-47.
[41] Jiang W-G, Hallett S, Wisnom M. Development of Domain Superposition Technique for the Modelling of Woven Fabric Composites. Mechanical Response of Composites: Springer Netherlands; 2008. p. 281-91.
[42] Chamis CC. Mechanics of composite materials: Past, present and future. Journal of Composites Technology and Research. 1989;11(11):3-14.

[43] Ivanov DS, Lomov SV, Ivanov SG, Verpoest I. Stress distribution in outer and inner plies of textile laminates and novel boundary conditions for unit cell analysis. Composites Part A: Applied Science and Manufacturing. 2010;41(4):571-80.
[44] Le Bozec Y, Kaang S, Hine PJ, Ward IM. The thermal-expansion behaviour of hot-compacted polypropylene and polyethylene composites. Composites Science and Technology. 2000;60(3):333-44.
[45] Jung-Ryul L, Molimard J, Vautrin A, Surrel Y. Application of grating shearography and speckle shearography to mechanical analysis of composite material. Composites Part A: Applied Science and Manufacturing. 2004;35A(7-8):965-76.
[46] Jung-Ryul L, Molimard J, Vautrin A, Surrel Y. Digital phase-shifting grating shearography for experimental analysis of fabric composites under tension. Composites Part A: Applied Science and Manufacturing. 2004;35A(7-8):849-59.
[47] Nicoletto G, Anzelotti G, Riva E. Mesoscopic strain fields in woven composites: Experiments vs. finite element modeling. Opt Laser Eng. 2009;47(3–4):352-9.
[48] Lomov S, Bogdanovich AE, Ivanov D, Hamada K, Kurashiki T, Zako M, et al. Finite element modelling of progressive damage in non-crimp 3D orthogonal weave and plain weave E-glass composites. In: Proceedings of 2nd World Conference on 3D Fabrics. Greenville, USA, Conference, Conference 2009.